

The Emission Structure of Formaldehyde MegaMasers

Willem A. Baan^{1,2}, Tao An^{2,1,3}, Hans-Rainer Klöckner⁴, and Peter Thomasson⁵

¹*Netherlands Institute for Radio Astronomy ASTRON, 7991 PD Dwingeloo, The Netherlands*

²*Shanghai Astronomical Observatory, Chinese Academy of Sciences, 200030 Shanghai, China*

³*Key Laboratory of Radio Astronomy, Chinese Academy of Sciences, 210008 Nanjing, China*

⁴*Max Planck Institut für Radioastronomie, 69 Auf den Hügeln, 5300 Bonn, Germany*

⁵*University of Manchester, Jodrell Bank Observatory, Macclesfield, Cheshire SK11 9DL, UK*

Accepted xxx. Received xxx; in original form xxx

ABSTRACT

The formaldehyde MegaMaser emission has been mapped for the three host galaxies IC 860, IRAS 15107+0724, and Arp 220. Elongated emission components are found at the nuclear centres of all galaxies with an extent ranging between 30 to 100 pc. These components are superposed on the peaks of the nuclear continuum. Additional isolated emission components are found superposed in the outskirts of the radio continuum structure. The brightness temperatures of the detected features ranges from 0.6 to 13.4×10^4 K, which confirms their masing nature. The masing scenario is interpreted as amplification of the radio continuum by foreground molecular gas that is pumped by far-infrared radiation fields in these starburst environments of the host galaxies.

Key words: Stars: formation – ISM: molecules – Radio lines: ISM – Masers – Galaxies: ISM – Galaxies: individual: IC 860, IRAS 15107+0724, Arp 220

1 INTRODUCTION

High-luminosity MegaMaser (MM) emission has been detected in external galaxies for four molecular species. Hydroxyl (OH) masers are found in the nuclear regions of Ultraluminous Infrared Galaxies ((U)LIRGs) (Baan et al. 1982), water vapour (H₂O) masers in accretion disks of active galactic nuclei (AGN) (Braatz et al. 2010; Kuo et al. 2015) and in interaction regions of jets and circumnuclear clouds (e.g., Claussen et al. 1984; Haschick & Baan 1985; Middelberg et al. 2007), formaldehyde (H₂CO) masers in the nuclear regions of ULIRGs (Baan et al. 1986; Araya et al. 2004), and recently methanol (CH₃OH) and Silicon Oxide (SiO) maser emission has been found in the starburst regions of (U)LIRGs as well as in nuclear feedback regions (Ellingsen et al. 2014; Chen et al. 2015; Wang et al. 2014).

A significant contribution to these observed molecular emissions may result from the amplification of the embedded or background radio continuum emission by foreground pumped molecular gas, as already proposed for the prototype OH MM source Arp 220 (IC 4553 - IRAS 15234+2354) (Baan et al. 1982). Rather than relying on the conventional high-gain maser scenario with a tunnel-like column of inverted molecules that amplifies some spontaneous seed emission, a large fraction of these OH MM emissions is produced by low-gain unsaturated amplification of the background radio continuum (Baan 1985). This scenario naturally accounts for the superposition of maser emission originating

in molecular cloud structures with variable local pumping conditions and the extended radio continuum in the source (Baan 1989; Parra et al. 2005), resulting in both low- and high-brightness maser components.

Superposition of maser and continuum sources has already clearly been shown for the powerful OH MM sources such as Arp 220 (e.g., Baan et al. 1987), Mrk 273 (e.g., Klöckner & Baan 2004), and IRAS 17207–0054 (e.g., Momjian et al. 2006), as well as for the strong central components of the H₂O MM source NGC 4258 (Miyoshi et al. 1995; Herrnstein et al. 1997) and other powerful sources such as NGC 3079 having an extended nuclear continuum structure (e.g., Haschick et al. 1990; Kondratko et al. 2005). Both the Class I and II methanol MM emissions observed in nearby starburst galaxies also suggest that they are confined within the extended continuum emission (Ellingsen et al. 2014; Chen et al. 2015). A first map of the formaldehyde emission in Arp 220 also shows a superposition of line emission and continuum (Baan & Haschick 1995) and the current study should confirm this composite maser amplification scenario. Similarly, Galactic OH and H₂O maser sources lose much of their flux at long terrestrial and space interferometer baselines, indicating the contribution of extended low-brightness maser emission (Slysh et al. 2001).

Formaldehyde masing activity remains very rare in the Galaxy and in extragalactic sources, and the observed masers are relatively weak and difficult to find. Although

formaldehyde absorption is widespread in the Galaxy, formaldehyde emission in the 4.829 GHz $K_a = 1_{10}-1_{11}$ transition is currently known to occur in only eight Galactic sources (e.g., [Araya et al. 2008](#); [Ginsburg et al. 2015](#)). The H_2CO MM emission in the extragalactic sources IC 860 and IRAS 15107+0724, and Arp 220 have been confirmed ([Baan et al. 1993](#); [Araya et al. 2004](#); [Mangum et al. 2008](#)), while other sources require interferometric confirmation. In addition, the source NGC 6240 displays two emission components that probably coincide with lower brightness continuum structures and that cover the velocity range of the single-dish spectrum ([Baan et al. 1993](#); [Wang et al. 2014](#)). While most extragalactic sources show absorption in both the 4.83 GHz $K_a = 1_{10}-1_{11}$ and the 14.5 GHz $K_a = 2_{11}-2_{12}$ transitions ([Mangum et al. 2013](#)), the few sources with ground-state emission also exhibit dominant absorption in the 14.5 GHz transition except for possible partial infilling of the line by emission. The current study suggests that the localised emission in the ground state may also be accompanied by more distributed absorption. The detection of such weak localised emission components embedded within more extended absorption requires higher resolution observations.

The masering activity in extragalactic sources strongly depends on the availability of an appropriate pumping agent for the molecular species and favourable environmental conditions. The known OH MM emissions generally occur in (U)LIRGs where radiative pumping of the OH results from star-formation induced dust infrared emissions ([Baan 1989](#); [Henkel & Wilson 1990](#); [Darling & Giovanelli 2002](#)). Since all three H_2CO MM sources are also known as OH MMs, it may be assumed that the infrared radiation fields in the nuclei of these galaxies also contribute to the pumping of the formaldehyde.

Issues to be raised in this study of IC 860, IRAS 15107+0724, and Arp 220 are the spatial structure of the masering formaldehyde emission components, their superposition on the nuclear continuum emission and their velocity characteristics. The observed brightness temperature of these components and the radio continuum will be used to confirm the masering nature of the line emission. This paper will also address the ability of the infrared radiation field to pump the masering activity of formaldehyde and to provide sufficient gains. A final issue to be considered is to seek evidence of more extended absorption in these sources.

2 MERLIN OBSERVATIONS

The 4.83 GHz H_2CO $K_a = 1_{10}-1_{11}$ transition data for the sources IC 860 (IRAS 13126+2452), IRAS 15107+0724 and Arp 220 (IRAS 15234+2354) have been obtained with the MERLIN array using the antennas at Defford, Cambridge, Knockin, Darnhall, Jodrell Mk2, Lovell, and Tabley.

IC 860 was observed from November 2009 for a total of approximately 35 hours including the flux density calibrator, 3C 286 (7.57 Jy), and the phase reference source, 1318+225 (0.26 Jy). The total target on-source time was 23.4 hrs, part of which was affected by weather. IRAS 15107+0724 was also observed during November 2009 for a total of 36.7 hours including the flux calibrator, 3C 286, baseline calibrator, OQ 208 (0.99 Jy), and phase reference source, 1509+054

Table 1. The Continuum Components

Source Component	RA ^a (s)	Dec ^a (^{''})	Continuum Flux (mJy/b)	Brightness Temperature (10 ⁴ K)
IC 860				
C	03.505	07.791	4.68	5.13
E	03.516	07.755	0.61	0.45
S	03.500	07.575	0.78	0.63
W	03.498	07.820	1.75	0.78
NW	03.497	07.946	0.75	0.12
IRAS 15107+0724				
C	13.094	31.872	7.92	9.40
NW	13.091	32.030	0.72	0.53
W	13.083	31.847	0.47	0.34
SW	13.088	31.616	0.48	0.35
S	13.095	31.587	0.56	0.41
SE	13.103	31.823	0.37	0.27
Arp 220				
W	57.094	31.876	30.42	30.2
E	57.091	32.030	13.38	13.3

Notes: (a) Positions of IC 860 are relative to RA = 13^h15^m and Dec = +24°37'. Positions of IRAS 15107+0724 are relative to RA = 15^h13^m and Dec = +07°13'. Positions for Arp 220 are relative to RA = 15^h34^m and Dec = +23°30'.

(0.84 Jy). The target on-source time was 27.1 hrs, part of which was also affected by weather. The observations of both IRAS 15107+0724 and IC 860 have an observing bandwidth of 16 MHz centred at a sky frequency of 4768.4 MHz, which corresponds to a redshift at band centre for both sources of 3802.8 km s⁻¹.

The heliocentric radial velocity of 3347 km s⁻¹ for IC 860 indicates a distance of 46.0 Mpc and a spatial scale of 223 pc/arcsec. The emission from IC 860 has been found to be close to its systemic velocity of 3911 km s⁻¹ and not at the heliocentric velocity of 3347 km s⁻¹ found in the literature. The heliocentric radial velocity of 3897 km s⁻¹ for IRAS 15107+0724 indicates a distance 53.8 Mpc and a spatial scale of 261 pc/arcsec.

The observations for Arp 220 were obtained in May 2004 and lasted for a total of 32 hrs with a target on-source time of 24.6 hrs. The flux density calibrator used was 3C 286 (7.60 Jy), the baseline calibrator was OQ 208 (0.99 Jy), and the phase reference source were 1511+238 (0.80 Jy) and 1530+239 (0.28 Jy). The observations for Arp 220 had an observing bandwidth of 16 MHz centred at a frequency of 4744.4 MHz giving a centre velocity of 5292.6 km s⁻¹ close to the peak velocity in the single-dish spectrum of 5430 km s⁻¹. For Arp 220 at a radial velocity 5375 km s⁻¹ and distance of 73 Mpc, the conversion from angular size to projected linear size is 356 pc/arcsec. The projected separation between the two continuum peaks in Arp 220 is 0.9 arcsec or 321 pc ([Sakamoto et al. 2008](#)).

The data reduction procedure followed the standard AIPS routines for flagging, calibration, bandpass calibration, self-calibration of phase calibrator, and imaging. The incremental phase and amplitude corrections obtained from the nearby phase calibrators were applied to the target source before imaging. The 31 channels in the observ-

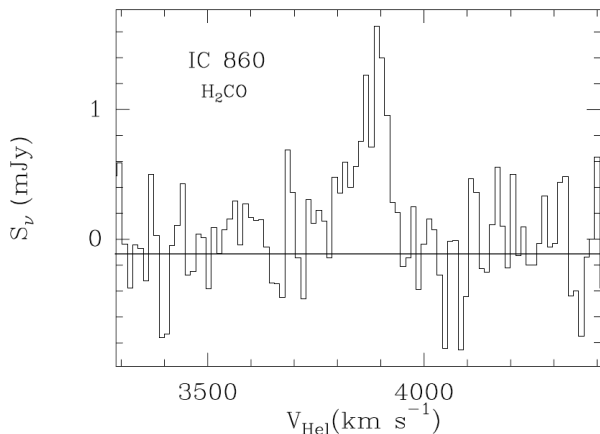


Figure 1. A single-dish spectrum of the formaldehyde emission in IC 860 obtained at 4.83 GHz with the Arecibo radio telescope in 1993 (Araya et al. 2004).

ing bands had a channel width of 0.5 MHz, which corresponds to a velocity resolution of approximately 31.04 km s^{-1} . The synthesized beam for IC 860 is $0.081'' \times 0.058''$ ($18 \text{ pc} \times 13 \text{ pc}$) and $0.101'' \times 0.071''$ ($26 \text{ pc} \times 18 \text{ pc}$) for IRAS 15107+0724. For Arp 220 the corresponding channel velocity resolution is 31.06 km s^{-1} and the synthesized beam size of Arp 220 is $0.079'' \times 0.068''$ ($25 \text{ pc} \times 23 \text{ pc}$).

The continuum structure of the sources has initially been obtained from the bandpass-corrected data cube by averaging two or three channels at the edge of the cube that show no evidence of the remaining bandpass structure and no discernible line emission. However, in order to obtain more accurate outer contours of the continuum structure, the centre 75% of the channel maps have been used to represent the continuum structure for IC 860 and IRAS 15107+0724, which then includes the weak line emission at the centre locations. The peak of the line emission for Arp 220, and also IC 860 and IRAS 15107+0724, is found to be close to the centre of the band and the line emission in the centre channels has been obtained by subtraction of a flat continuum structure based on the edge channels across the whole cube. A flat baseline subtraction does not remove any existing channel structure in the band and only brings the continuum level close to zero. Only for the final results for IC 860 the continuum subtraction was based on only the low frequency edge channels in order to take into account the possible line emission near the high frequency edge. For Arp 220 the emission extends beyond the edge of the observing band, which may result in errors in the continuum subtraction. A larger observing band of these MERLIN observations would have helped to take away any uncertainty continuum subtractions.

The formaldehyde line emission features in all three sources are known to be very weak from single-dish observations (e.g., Araya et al. 2004) and special attention has been paid during the data reduction process in order to arrive at reliable results. Some of the data has also been reduced using Miriad, which produced the same results. Simple tests such as determining the emission structures by stacking the emission line channels also produced the same results as using moments. There is no evidence that any of the observed

weaker features away from the nuclear region result from imperfect data reduction. All emission features in the maps are indeed found to be superposed on the radio continuum contours of the sources.

The results of the current studies show some differences between line profiles obtained from the interferometric data and those obtained with single-dish experiments. Some differences may result from residual errors in calibration and continuum subtraction using a limited number of line-free edge channels. In addition, the presence of diffuse absorption against the radio continuum may account for differences when sampled with different beam sizes.

The analysis of the three target sources requires an evaluation of the observed brightness temperatures of the formaldehyde spectral components and the continuum structures. The brightness temperatures of a source component may be determined as (Kellermann & Owen 1988):

$$T_b = 1.22 \times 10^{12} S_\nu (\theta_{\text{maj}} \theta_{\text{min}} \nu^2)^{-1} (1+z) \text{ K}, \quad (1)$$

where the observing frequency ν is in unit of GHz, the component flux density S_ν has a unit of Jy, the source sizes θ_{maj} and θ_{min} are in milli-arcseconds.

In this paper, distances were determined using a cosmological model with $H_0 = 73 \text{ km s}^{-1} \text{ Mpc}^{-1}$, $\Omega_M = 0.27$ and $\Omega_\Lambda = 0.73$ (Spergel et al. 2007).

3 FORMALDEHYDE IN IC 860 - IRAS 13126+2452

3.1 IC 860 - Formaldehyde Emission

The 4.83 GHz formaldehyde $K_a = 1$ emission in IC 860 - IRAS 13126+2452 has first been observed with the Arecibo Observatory with a peak flux density of 2.0 - 2.2 mJy (Baan et al. 1993). A representative spectrum shows an asymmetric profile centred at 3860 km s^{-1} with a total width of 160 km s^{-1} as presented in Figure 1 (from Araya et al. 2004). IC 860 also exhibits HI absorption centred at 3866 km s^{-1} as well as a combined OH spectrum with absorption at 3850 km s^{-1} and emission at 4000 km s^{-1} (Schmelz et al. 1986). These spectra of IC 860 cover a total velocity range from 3700 to 4100 km s^{-1} . Similarly, the formaldehyde spectrum of IC 860 may also extend from 3550 to 4100 km/s with a weak emission feature at 3580 km s^{-1} and weak absorption features at 3700 and 4050 km s^{-1} . This signature may also be recognised in the spectrum obtained with the Green Bank Telescope (Mangum et al. 2013). These weak features may be further verified using single-dish or interferometric data.

The formaldehyde line emission structure of IC 860 is presented in Figure 2 as a zeroth-moment colour map overlaid on the radio continuum map. The moment map incorporates line emission features above a threshold of $0.8 \text{ mJy beam}^{-1}$, while the rms in the line channel maps (away from the location of the source) is $0.31 \text{ mJy beam}^{-1}$. The central line emission region extends 31 pc at $\text{PA} = 130^\circ$ with an additional extension to the east at $\text{PA} = 270^\circ$. The region is centred on the nuclear continuum peak and its orientation agrees well with that of the 2Mass image of the galaxy of $\text{PA} = 150^\circ$ (Skrutskie et al. 2006) and lies perpendicular to the northwest continuum extension. One weaker and significant

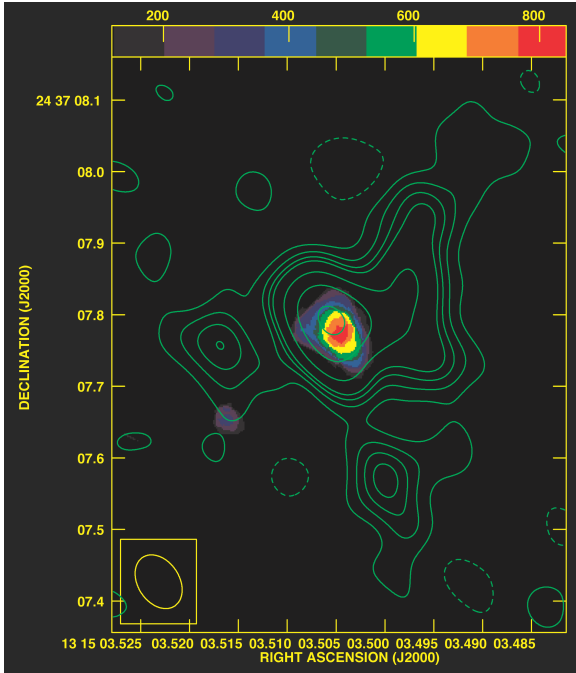


Figure 2. The H_2CO emission structure superposed on the nuclear continuum structure of IC 860. The contoured continuum emission structure has a peak flux density of $6.42 \text{ mJy beam}^{-1}$, which includes the weak line emission. The actual continuum peak intensity is $4.68 \text{ mJy beam}^{-1}$. The continuum contour levels are $0.18 \text{ mJy beam}^{-1} \times (-1, 1, 2, 3, 4, 8, 16, 32)$ with a rms noise in the map of $0.077 \text{ mJy beam}^{-1}$. The moment 0 map of the H_2CO emission structure is presented as a colour map with a range of $120\text{--}840 \text{ mJy beam}^{-1} \text{ km s}^{-1}$. Two emissions components are found in the map as the prominent Centre region and the weaker SouthEast region. The integrated peak of the Centre line emission converts to $1.74 \text{ mJy beam}^{-1}$.

emission feature, SouthEast of the nucleus, is found in the zeroth-moment map inside the continuum contours.

The underlying continuum structure of the nuclear region of IC 860 consists of a compact component and extended components towards the northwest, the southwest, and to the east. With an integrated flux density 15.31 mJy , the compact component has a peak flux density of $4.68 \text{ mJy beam}^{-1}$. The brightness temperatures, T_b , of the central component ($5.13 \times 10^4 \text{ K}$) and the other components (in the range 0.45 to $0.78 \times 10^4 \text{ K}$) are consistent with the occurrence of star formation in all continuum components (Condon 1992). In order to better define the outer continuum structure, the (weak) line emission close to the nuclear centre has been included in the continuum map in Figure 2, which results in an increased peak flux density of $6.42 \text{ mJy beam}^{-1}$. The parameters for the nuclear and circumnuclear components are presented in Table 1.

3.2 IC 860 - Formaldehyde Emission Structure

The channel maps of the line emission for IC 860 have been presented in Figure 3. The negative (single solid line) contours indicate the general noise level of each of the maps as well as the location of (extended) structures possibly repre-

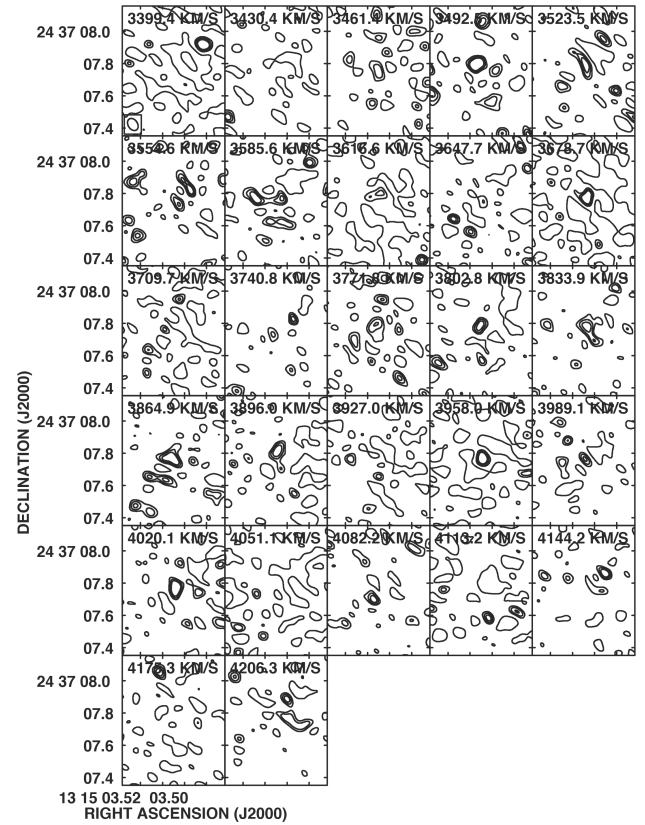


Figure 3. Channel maps of IC 860. The contour levels for the 27 central channels emphasise the negative (single solid line) contours as well as the strongly positive (multiple concentric) contours of the maser emission features. The contour levels are $0.5 \text{ mJy beam}^{-1} \times (-1, 1, 2, 3)$ such that the extended single contours are negative.

senting weak absorption against the radio continuum of the source. The features with multiple positive contours identify the emission features located within the contours of the radio continuum. These features have the approximate size of the resolving beam and represent very localised emission regions with single or multiple maser sources that often fill a single spectral channel in the maps. Features above the second positive contour have been added to the Moment 0 map in Figure 2.

The first moment map of the central emission components in IC 860 does not show a distinct velocity gradient (Fig. 4). Instead the colour contours indicate a dominant emission component with a velocity in the range $3730\text{--}3820 \text{ km s}^{-1}$ superposed on some larger scale background velocity structure with 3500 km s^{-1} at the East and West edges and 3850 km s^{-1} in the North and South.

3.3 IC 860 - Spectral Characteristics

The integrated spectral profile of the H_2CO line emission in the nuclear Centre region of IC 860 is presented in Figure 5(a) and shows three distinct emission components. The features centred at 3830 and 3990 km s^{-1} (ranging from 3720 - 4050 km s^{-1}) are in rough agreement with the single-dish emission components peaking at 3890 km s^{-1} in Figure

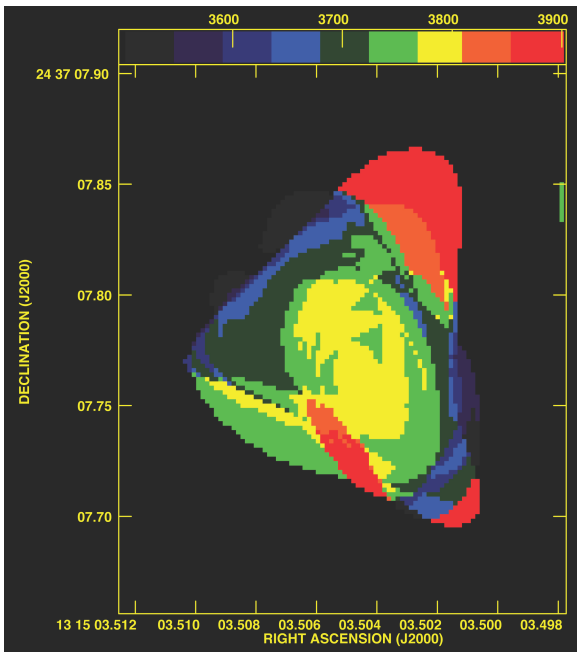


Figure 4. The velocity structure of the central H_2CO emission structures of the nuclear region of IC 860. The first moment map shows colour contours between 3500 and 3900 km s^{-1} . The velocity structure may reveal a superposition of point sources but does show an overall velocity gradient.

1, although the high-velocity edge is less prominent in the single-dish spectrum. The broad feature at 3590 km s^{-1} with a mean flux of $0.95 \text{ mJy beam}^{-1}$ (line width of 230 km s^{-1}) only has a weak counterpart in the single-dish spectrum. The integrated spectrum of the SouthEast region is displayed in Figure 5(b). This spectrum shows emission peaks at 3700 and 3880 km s^{-1} but also the smaller feature at 3580 km s^{-1} that is also found in the Centre region.

In addition to the main emission features seen in the single-dish spectrum of Figure 1, the emission component close to 3580 km s^{-1} does not have a strong counterpart in the single-dish spectrum and occurs precariously close to the edge of the observing band. Careful inspection of the data reduction procedure shows that this emission is not the result the bandpass calibration or the flat continuum subtraction using the edge channels. (A great effort has been done to make this feature disappear but it would not.) While the strength of this emission component remains unexpected, we suggest that the feature really exists and is compensated in the single-dish spectrum by absorption in the nuclear region in certain channels.

The systemic velocity of IC 860 is nominally at 3347 km s^{-1} (Haynes et al. 1997), but all known OH and HI emission and absorption features are found close to a higher velocity of 3911 km s^{-1} . While the 2Mass image does not show clear signs of a galaxy interaction (Skrutskie et al. 2006), these two velocities may indicate the interactive nature of the IC 860 system consistent with its large FIR luminosity. The observed velocity component at 3580 km s^{-1} would be consistent with the maser emissions occurring closer to the systemic velocity.

Close to the peak of the continuum emission in Figure 2,

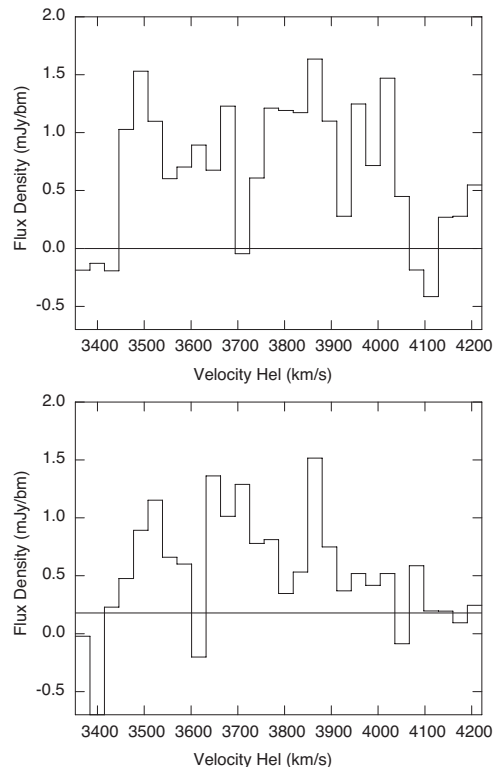


Figure 5. The integrated spectra of the formaldehyde emission in IC 860 integrated of the Centre emission region and the South-East region. (top) The Centre region exhibits three distinct velocity components at $V = 3590, 3830,$ and 3990 km s^{-1} . The 3590 km s^{-1} component has a weak counterpart in the single-dish spectrum of Fig. 1, while the other components find their counterparts in the main feature of the single-dish spectrum and a possible high velocity wing. (bottom) The spectrum at the South-East region shows three distinct components at shifted velocities of $V = 3520, 3720$ and 3870 km s^{-1} .

the estimated amplifying optical depths for the spectral features vary as $\tau = 0.34\text{--}0.46$ and the brightness temperatures range from 3.0 to $5.2 \times 10^4 \text{ K}$. The spectral components in the weaker SouthEast region show an optical depth ranging from 1.11 to 1.90 with brightness temperatures ranging from 2.2 to $4.2 \times 10^4 \text{ K}$ (Table 2). The regions with the highest flux densities and the lowest gains are located towards the peak of the continuum distribution, which is consistent with a stronger background requiring a lower amplifying gain.

The distinct components at the centre and SouthEast locations between 3650 and 4000 km s^{-1} contribute to emission in the integrated single-dish spectrum (Fig. 1). A superposition of the emission (and possible absorption) across the face of the nuclear continuum could account for the differences between the single-dish spectrum and the current MERLIN spectra. However, the reality of the weak emission feature at 3580 km s^{-1} in the single-dish spectrum and the feature found in the current data does require further verification with more sensitive observations having a larger observing bandwidth.

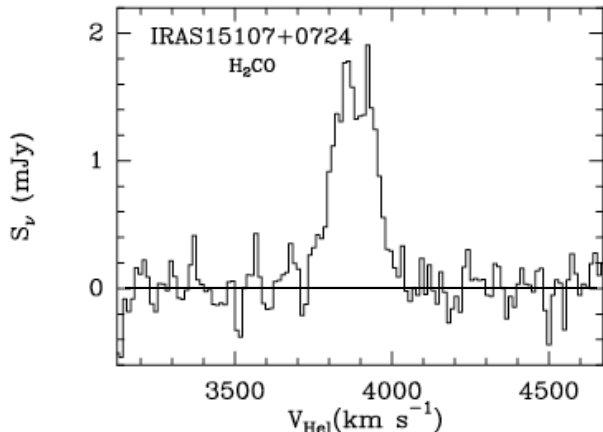


Figure 6. A single-dish spectrum of IRAS 15107+0724 obtained with the Arecibo radio telescope. Taken from (Araya et al. 2004)

4 FORMALDEHYDE IN IRAS 15107+0724

4.1 IRAS 15107 - Formaldehyde Emission

IRAS 15107+0724 has been first detected at Arecibo Observatory (Baan et al. 1993) with a peak flux of 1.91 mJy. A representative spectrum, presented in Figure 6 (Araya et al. 2004), shows a spectral line with a mean velocity of 3880 km s^{-1} and a total width of 320 km s^{-1} , but clearly consisting of two components. No other tentative features can be seen in the spectrum. An OH spectrum also shows two emission components centred at 3782 and 3900 km s^{-1} , whereas the HI spectrum shows a broad absorption feature centred at 3902 km s^{-1} (Baan et al. 1987). The galaxy itself has a systemic velocity of 3897 km s^{-1} .

The formaldehyde line emission in IRAS 15107+0724 is presented as a zeroth moment colour overlay on the continuum contours in Figure 7. The line channels in the data cube have a rms noise of $0.17 \text{ mJy beam}^{-1}$ and the moment maps incorporate signals above a flux threshold of $0.4 \text{ mJy beam}^{-1}$. The main emission feature straddles the central continuum peak and has an extent of 52 pc at $\text{PA} = 140^\circ$. This orientation agrees well with the orientation of the 2Mass image of the galaxy at $\text{PA} = 155^\circ$ (Skrutskie et al. 2006). Two other compact emission regions, South and NorthWest, are superposed on the extended radio continuum structure.

The underlying continuum structure of IRAS 15107+0724 shows a central nuclear component surrounded by a ring of emission tracing two inner spiral arms and resembling an S-shaped structure (Fig. 7). The total flux density of the source is 29.72 mJy with a peak of $12.57 \text{ mJy beam}^{-1}$. The brightness temperature at the nuclear source is $9.4 \times 10^4 \text{ K}$, while the peaks in the surrounding structure have brightness temperatures in the range $(0.27\text{-}0.53) \times 10^4 \text{ K}$. These temperatures and the emission structure support the hypothesis that this entire S-shaped continuum structure traces star formation activity, although the presence of an embedded radio AGN at the nucleus cannot be excluded. In order to better define the outer continuum structure, the contour map presented in Figure 7 also includes the central line emission. The

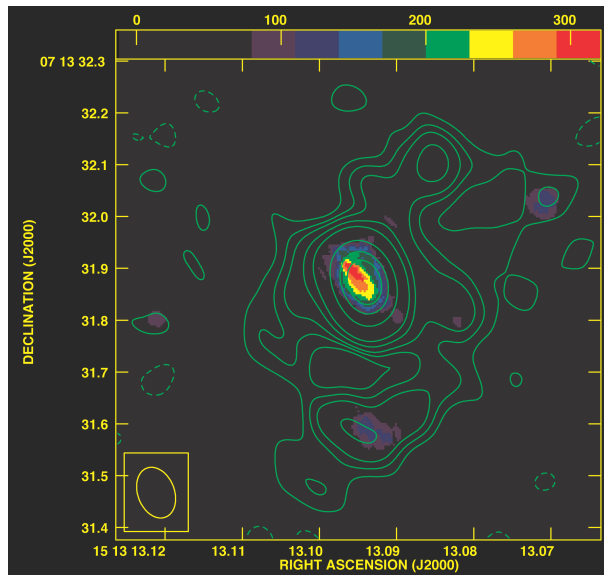


Figure 7. The formaldehyde line emission and radio continuum structure of the IR 15107+0724. A continuum source shows a central component with a peak flux of 7.92 mJy/beam surrounded by distributed emission regions resembling a ring or inner spiral arms. The contour levels are $0.11 \text{ mJy/beam} \times (-1, 1, 2, 3, 5, 8, 24, 48, 72)$. The rms in the continuum map is 0.051 mJy/beam . The zeroth moment of the formaldehyde emission is presented as a superposed colour scale map. The peak integrated flux is 308.8 mJy*km/s and the colour scale runs from 60 to 320 mJy*km/s . Three distinct emission regions are found within the continuum contours at the Centre position and at the South and NorthWest positions.

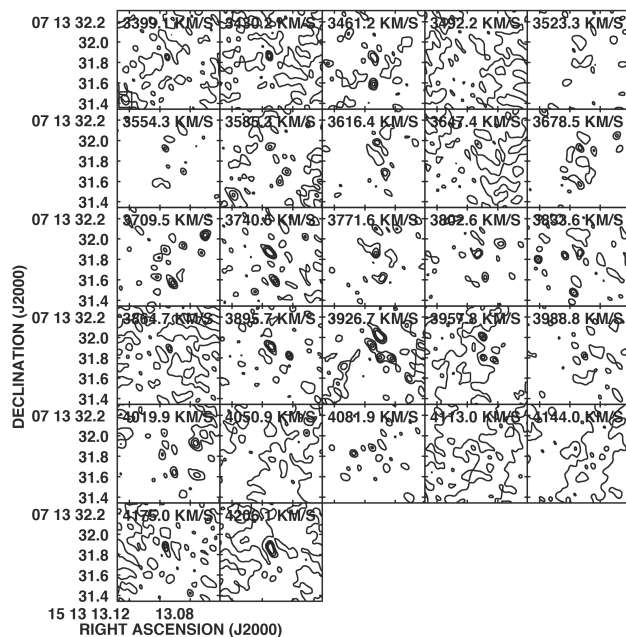


Figure 8. Channel maps of IR 15107+0724. The contour levels for the 27 central channels emphasize the negative (single solid line) contours as well as the strongly positive (multiple concentric) contours of the maser emission features. The contour levels are $0.2 \text{ mJy beam}^{-1} \times (-2, 4, 6, 8)$.

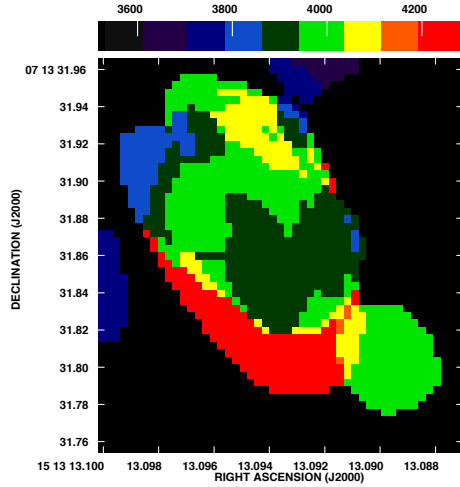


Figure 9. The velocity field of the formaldehyde emission region at the Centre of IRAS 15107+0724. The velocity colours in the first moment map range between 3750 and 4050 km s⁻¹. No clear organised motion can be seen across the Centre emission region except for a (possible) velocity gradient covering 250 km s⁻¹ from Northeast to Southwest. A dominant central component exists close to the systemic velocity of 3850 km s⁻¹ located close to the central continuum peak of the source. The emission and the associated velocity field seems dominated by a superposition of strong emission components.

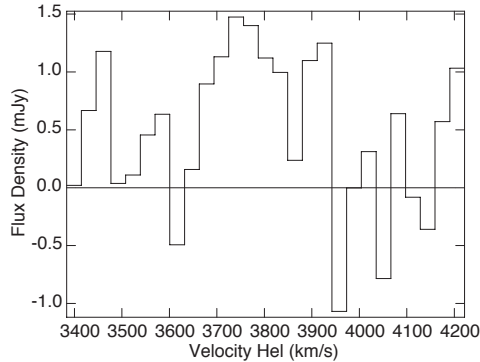


Figure 10. Integrated formaldehyde emission spectrum at the Centre position of IRAS 15107+0724.

positions, the continuum flux densities, and the brightness temperatures of these identifiable components are presented in Table 1.

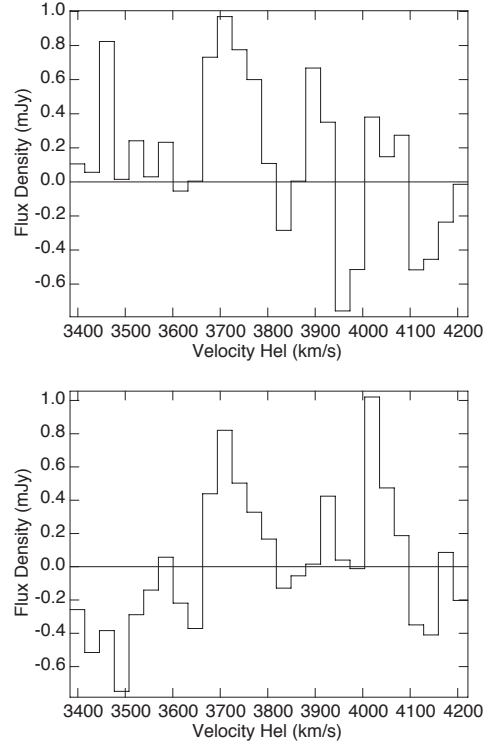


Figure 11. Integrated formaldehyde spectra at the two additional emission components of IRAS 15107+0724 at the Southern component (top), and the NorthWest component (bottom). The spectra suggest that there is also absorption in the source and that individual emission components exist within the observed range of 3650–4050 km s⁻¹ in the single-dish spectra (see Fig.6).

4.2 IRAS 15107 - Formaldehyde Emission Structure

The channel maps of the line emission for IR15107+0724 have been presented in Figure 8. The negative (single solid line) contours indicate the general noise level of each of the maps as well as the location of possible absorption features against the radio continuum of the source. The features with multiple positive contours identify the localised emission features in the maps lying mostly within the contours of the radio continuum. The features above the first positive contour have been presented in the Moment 0 map in Figure 7. The emission structure of formaldehyde in IR 15107+0724 is also made up of multiple (single) features that often fill only one spectral channel and are found across the centre of the velocity range. In addition, the presence of extended negative contours may be consistent with the concept that certain emission features are compensated by regions of absorption.

4.3 IRAS 15107 - Spectral Characteristics

The velocity field in the first moment map shows a semi-organized NE-SW velocity gradient (PA = 145°) across the nuclear emission region (Fig. 9) with a central dominant component at 3850 km s⁻¹ superposed close to the centre.

The spectral signature of the central emission compo-

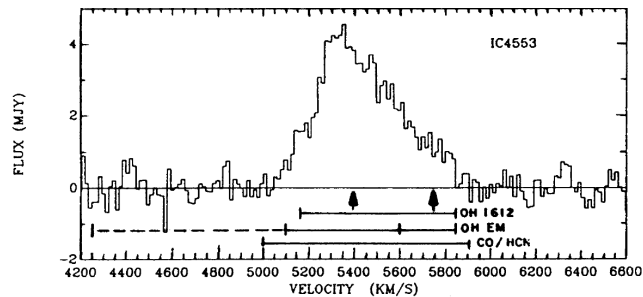


Figure 12. A single-dish spectrum of Arp 220 obtained with the Arecibo radio telescope. The two arrows indicate the systemic velocities of the West and East nuclei. The horizontal bars below the spectrum indicate the observed velocity range of the OH 1612 MHz absorption, the OH 1667/1665 MHz MM emissions, and the thermal CO(1-0) and HCN(1-0) emissions in the nuclear region. The dashed line indicates the range of the observed blueshifted OH outflow emission.

ment in the zeroth moment map in Fig. 7 has been presented in Figure 10. The central component contributes most to the integrated emission close to the systemic velocity with a peak at 3750 km s^{-1} , which is below the observed 3880 km s^{-1} velocity of the emission peak and the 3897 km s^{-1} systemic velocity. The spectra for the two weaker emission components, South and NorthWest, are presented in Figure 11. Both the South and NorthWest emission regions show additional velocity components below (3710 km s^{-1}) and above (4015 km s^{-1}) the systemic velocity of 3820 km s^{-1} . These coarse velocity designations are quite consistent with the velocities found at the Centre region, although the multiple velocity systems are reminiscent of a merger scenario.

The characteristics of all emission regions within the continuum confines of IRAS 15107+0724 have been presented in Table 2. The peak line flux density at the nucleus is $1.45 \text{ mJy beam}^{-1}$ and the integrated fluxes at the three other regions are in the range $0.45 - 1.0 \text{ mJy beam}^{-1}$. The central line emission regions in IRAS 15107+0724 superposed on the continuum peak have a brightness temperature in the range of 3.4 to $4.2 \times 10^4 \text{ K}$ and apparent optical depths of only 0.16 to 0.20 (see Table 2). The line emission features in the two other features have brightness temperatures higher than those of the radio continuum ranging from 0.6 to $4.0 \times 10^4 \text{ K}$ and they have higher optical depths ranging from 0.44 to 1.71 . Although some larger optical depths are found, both the brightness temperatures and the deduced optical depths are consistent with modelling results with radiative pumping schemes (details in Sect. 6.3).

The spectral features emission found in IRAS 15107+7024 (Fig. 10 and 11) cover the velocity range of the observed single-dish spectrum extending from 3650 to 4050 km s^{-1} with some of the weaker features covering the shoulders. The dropouts at higher velocities at the Southern location and at lower velocities at the NorthWest location appear unusual but they are found to be a local characteristic. They are not the result of continuum subtraction. These differences are consistent with the presence of weak absorption structures against the continuum structure that do not stand out clearly in the single-dish spectrum.

5 FORMALDEHYDE IN ARP 220 (IC 4553)

5.1 Arp 220 - Formaldehyde Emission

The extragalactic formaldehyde emission from Arp 220 was first detected using the Effelsberg telescope in 1984 together with the absorption lines in NGC 3628 and NGC 3079 (Baan et al. 1986). A representative Arecibo spectrum of the line has been presented in Figure 12 (from Baan et al. 1993). With a single-dish line strength of only $\sim 4.0 \text{ mJy}$ and an isotropic luminosity $L_{\text{H}_2\text{CO}} = 61 L_{\odot}$, it is the strongest and most luminous among the known H_2CO MMs (Araya et al. 2004). The formaldehyde emission is found to extend across the central molecular zones of each of the nuclei, while the peak of the formaldehyde spectrum at 5340 km s^{-1} is dominated by emission at the systemic velocity of the Western nucleus (Baan & Haschick 1995). Based on the OH MM emission at 1667 MHz and a number of high-density tracer molecular emissions (Baan 2007), the systemic velocities of the two nuclei are 5683 km s^{-1} for the Eastern nucleus and 5365 km s^{-1} for the Western nucleus. As a result the emissions at the systemic velocity of the Eastern nucleus do not fall within the frequency window of these observations.

The formaldehyde emission structures at the nuclei of Arp 220 are presented in Figure 13 as a zeroth moment formaldehyde emission colour map superposed on the continuum contours. These emission regions exhibit both discrete and extended components of different strengths superposed on the extended continuum structure of the West and the East nuclear regions. The dominating central emission structure at the West nucleus is elongated by 110 pc in a North - South direction and is similar to the elongated structures found at the nuclei of IC 860 and IR 15107+0724. However, the Western nucleus shows a more complex structure than just a North-South nuclear disc structure. Possibly the East-West structure with a distinct (east-west) velocity gradient represents a superposed structural component resulting from the ongoing merger. Alternatively, these are star formation regions away from the disc. The emission region at the Eastern nucleus covers approximately 53 pc and consists of two regions in Northeast - Southwest direction. It should be noted that this emission occurs at the systemic velocity of the Western nucleus, while emission at the systemic velocity of the Eastern nucleus falls at the upper edge (or outside) of the observing band.

The underlying continuum structure of the merger system Arp 220 in Figure 13 shows two isolated nuclei with peak flux densities of the East and West nuclei of 13.38 and $30.42 \text{ mJy beam}^{-1}$). The peak brightness temperatures at 4.83 GHz for the eastern and western nuclei are 1.3 and $3.0 \times 10^5 \text{ K}$, respectively (Table 1), which is consistent with intense star formation. The (loop-like) structure that extends southward from the western nucleus to the eastern nucleus has been resolved out at this higher resolution (Baan & Haschick 1995; Rovilos et al. 2003). The extended structures at various position angles would be evidence that the star formation extends into pre-existing spiral arms or larger scale structures within the merging nuclei. No evidence has been found yet for the presence of an AGN in either one of the nuclei (Smith et al. 1998; Genzel et al. 1998).

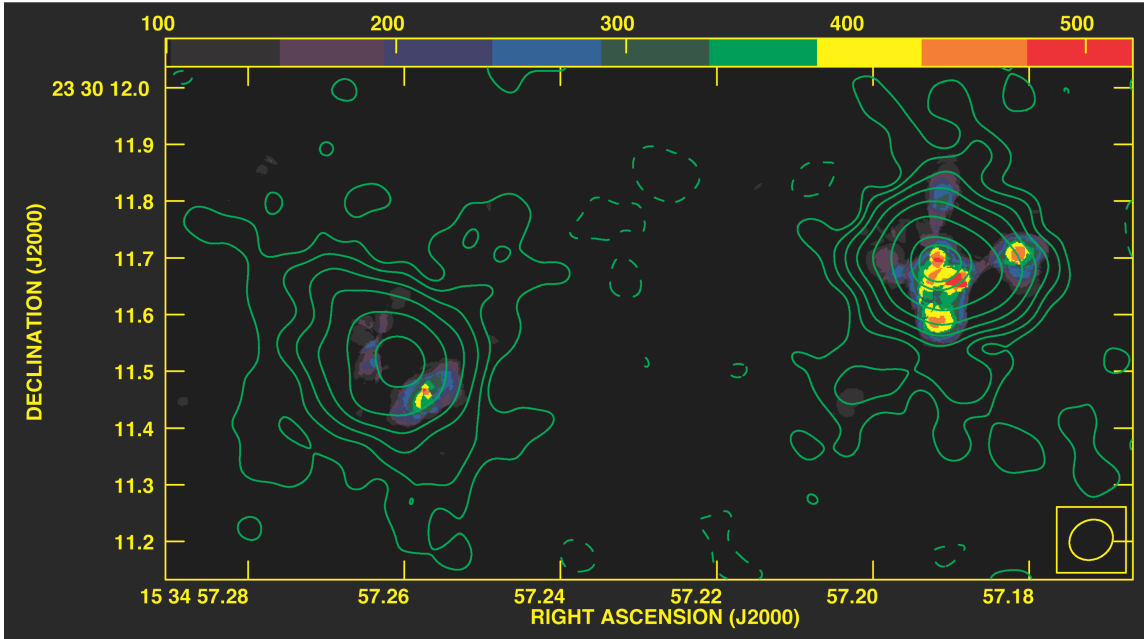


Figure 13. A composite map of the continuum emission and the formaldehyde line emission in Arp 220. The continuum structure is depicted with contours at levels $0.30 \times (-1, 1, 2, 4, 8, 16, 32, 64, 80)$ mJy beam⁻¹ and a peak flux of 30.42 and 13.38 mJy beam⁻¹ for the western and eastern nucleus, respectively. The colour scale zeroth moment image depicts a range of 0.1 to 0.56 mJy beam⁻¹ km s⁻¹. The line emission image show four emission regions at the Western nucleus: W-Centre, W-North, W-West, and W-South. The Eastern nucleus displays two line emission regions: E-West and E-East.

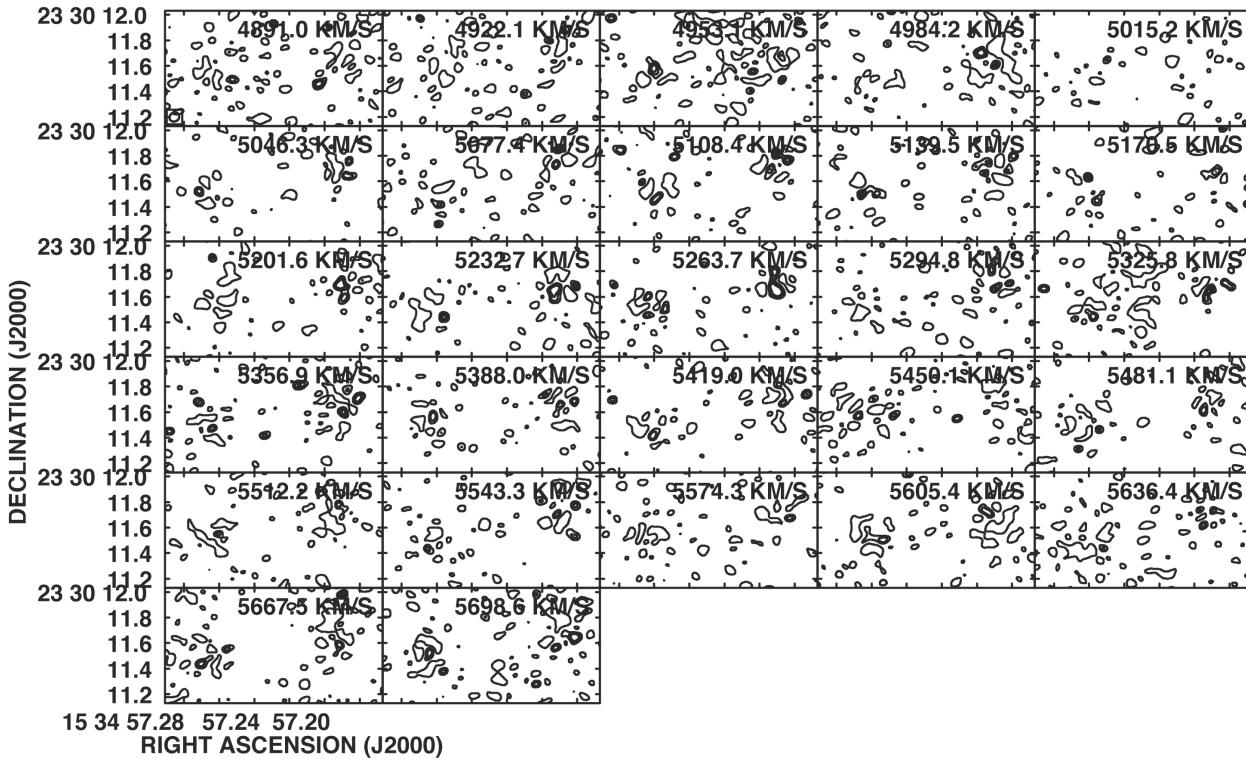


Figure 14. Channel maps of Arp 220. The contour levels for the 27 central channels indicate the negative (single solid line) contours as well as the strongly positive (multiple concentric) contours of the maser emission features. The contour levels are 0.3 mJy beam⁻¹ \times (-2, 4, 6, 8)

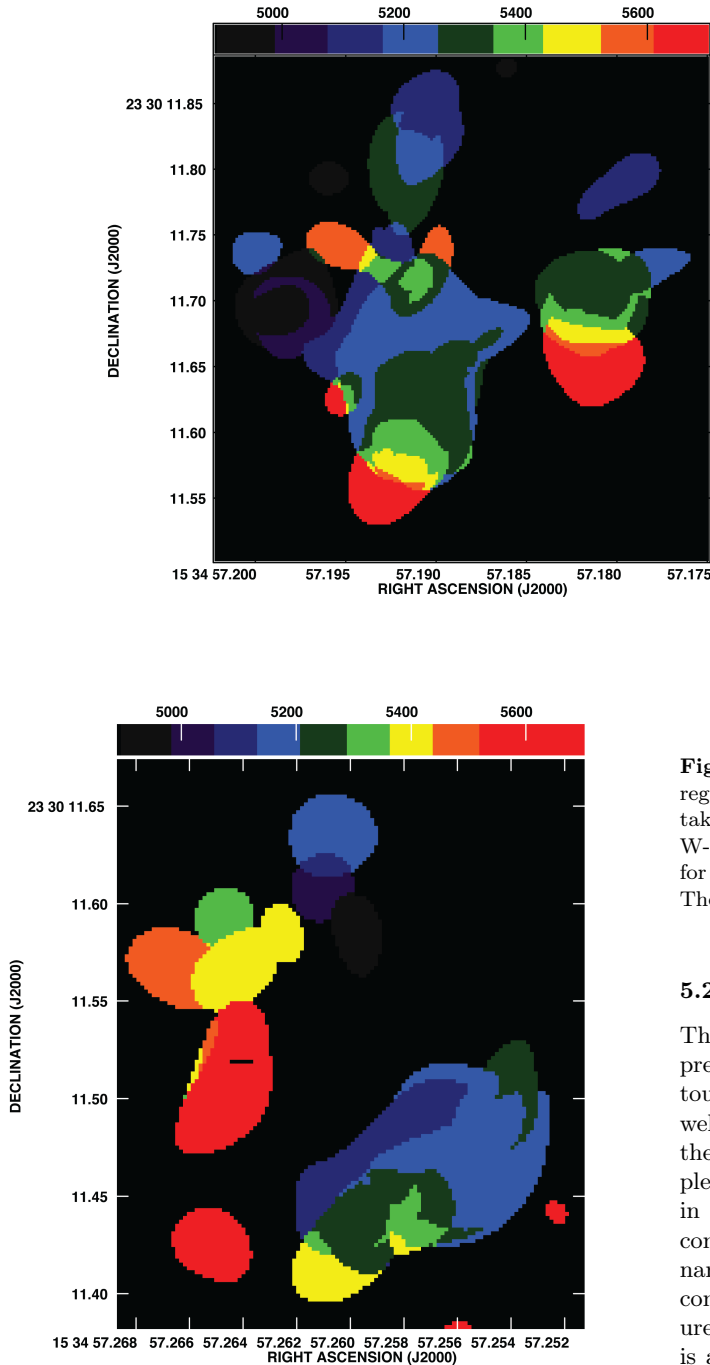


Figure 15. The velocity fields at the Western nucleus (top) and Eastern nucleus (bottom) of Arp 220. The emission regions in the Western nucleus possibly display a weak North - South velocity gradient and also the regions in the Eastern nucleus indicate a SouthWest - NorthEast gradient.

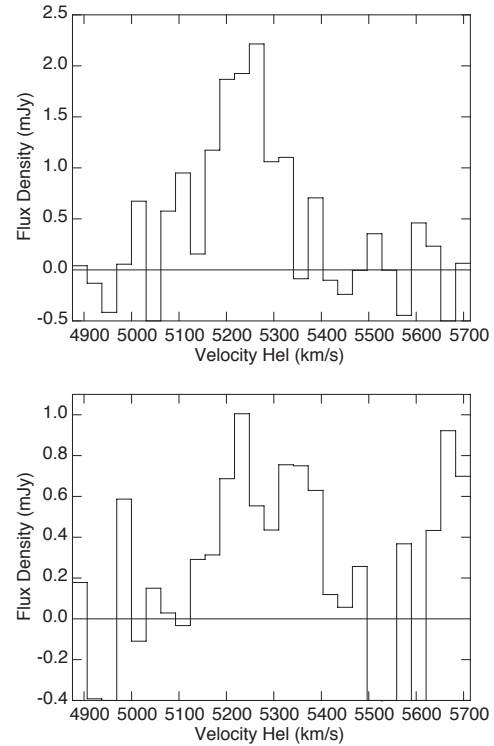


Figure 16. Integrated spectra resulting from the central emission regions in the Western nucleus of Arp 220. The spectra have been taken at northern part W-Centre (top) and at the southern part W-South (bottom). Together these emission components account for much the single-dish emission profile as presented in Fig. 12. The structure at 5650 km s^{-1}

5.2 Arp 220 - Formaldehyde Emission Structure

The channel maps of the line emission for Arp 220 have been presented in Figure 14. The negative (single solid line) contours indicate the general noise level of each of the maps as well as the location of possible absorption features against the radio continuum of the source. The features with multiple positive contours identify the localised emission features in the maps lying mostly within the contours of the radio continuum of the two nuclei. The features from the dominant emission regions in both nuclei above the first positive contour have been presented in the Moment 0 map in Figure 13. The emission structure of formaldehyde in Arp 220 is also made up of multiple (single) features that often fill only one spectral channel. They are also found across a large fraction of the velocity range, which does not fully cover the range of $5000 - 5850 \text{ km s}^{-1}$ of the observed emission from the two nuclei (see Fig. 12).

5.3 Arp 220 - Spectral Characteristics

The velocity field of the emissions at the two nuclei of Arp 220 has been presented in the first moment maps of Fig. 15. Because of the 300 km s^{-1} velocity difference between the two nuclei, the observed emission mostly covers the velocity range of the West nucleus. The weaker emission at the systemic velocity of the Eastern nucleus enters the band only above 5600 km s^{-1} . Both emission regions exhibit very

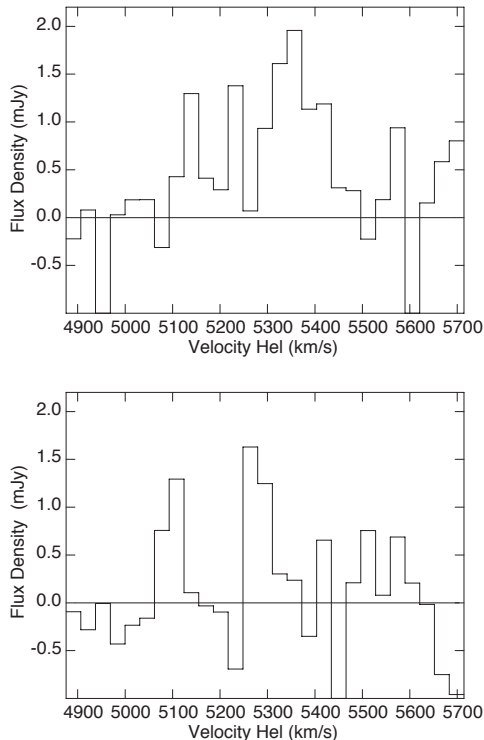


Figure 17. Integrated spectra resulting from the other emission regions in the Western nucleus of Arp 220. The spectra are those taken across the Western nuclear component W-West (top) and the Northern nuclear component W-North (bottom).

complex velocity fields that suggest that the observed emission represents a superposition of compact emission regions at different radial velocities. The emission regions at the West nucleus may show a possible North - South gradient at PA = 6° and centred at $V_{west} = 5365 \text{ km s}^{-1}$ across the W-North, W-Centre, and W-South regions. On the other hand, the W-West region shows higher velocities and the weaker W-East region shows lower velocities. The emission at the East nucleus has a velocity field also centred at the V_{west} velocity with a (possible) Southwest - Northeast gradient at PA = 315° across the regions. While the orientation of these velocity gradients are in rough agreement with those of the OH MM (1667 MHz) data, the velocity gradient at the West nucleus appears opposite to the local HI and OH gradient (Rovilos et al. 2003; Baan 2007). The whole nuclear region shows a North - South gradient based on CO and HCN molecular data (Downes & Solomon 1998; Zhao & An 2008; Sakamoto et al. 2008). Considering that the formaldehyde material seen at the East nucleus mostly belongs to the West galaxy and that the observed emission has a very complex structure, no detailed information can be derived from the velocity structure in the moment maps.

The line emission spectra of the four prominent components in the West nucleus (Fig. 16 and 17) and of two prominent components in the East nucleus (Fig. 18) show a complementary picture. The central emission regions W-Centre and W-South at the West nucleus at 5230 km s^{-1} provide the dominant peak in the single-dish spectrum while the emission from the western regions W-West contributes to

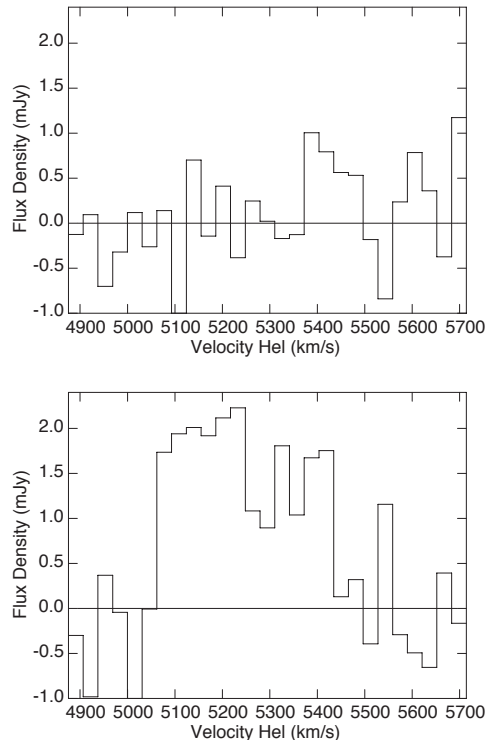


Figure 18. Integrated spectra resulting from emission regions at the Eastern nucleus of Arp 220. The spectra are those from the E-East region (top) and the E-West region (bottom).

the higher-velocity shoulder of the profile. Region W-North in the West nucleus also contributes to the lower velocity shoulder. The East nucleus in E-West shows multiple peaks covering a larger velocity range that contributes to both the low-velocity wing down to 5100 km s^{-1} and the extended high-velocity wing up to 5540 km s^{-1} . This higher velocity component at the East nucleus and also the 5600 km s^{-1} structure in the W-South location (16) are consistent with emission close to the systemic velocity of the East nucleus as has also been seen in the OH 1667 MHz MM data (Baan & Haschick 1984; Rovilos et al. 2003). The spectra at both nuclei as presented in Figures 16, 17 and 18 again show the presence of localised (narrow and broad) absorption-like features.

The amplifying optical depth and the brightness temperature of the emission line features in Arp 220 are presented in Table 2. The optical depth of the features at both nuclei varies between 0.10 and 0.29, with smaller values at locations with higher continuum fluxes, consistent with amplification of the continuum. The brightness temperatures of the features vary between 2.5 and $13.4 \times 10^4 \text{ K}$. The high brightness temperatures of all emission components confirm masering nature of these emissions.

6 INTERPRETING THE EMISSION

6.1 Extragalactic Emission Structures

The formaldehyde $K_a = 1_{10}-1_{11}$ data at 4.829 GHz in IC 860, IRAS 15107+0724, and Arp 220 confirms that the

Table 2. The line emission components

Source Component	RA ^a (s)	Dec ^a (^{''})	Continuum Flux ^b (mJy/b)	Velocity (km/s)	Line Flux (mJy/b)	Line Optical Depth ^c	Brightness Temperature T _b (10 ⁴ K)
IC 860							
Centre	03.504	07.79	4.04	3490, 3640, 3830, 3990	(3.30), 1.90, 2.80, 1.90	(0.62), 0.34, 0.46, 0.34	3.01 - 5.23
SouthEast	03.516	07.67	0.20	3520, 3720, 3870	0.71, 0.79, 1.34	1.26, 1.37, 1.90	2.23 - 4.16
IRAS 15107+0724							
Centre	13.097	31.92	6.61	3760, 3910	1.45, 1.18	0.20, 0.16	4.22, 3.43
South	13.093	31.58	0.50	3460, 3710, 3900,4050	0.80, 0.95, 0.66, 0.28	0.95, 1.06, 0.84, 0.44	0.56 - 1.92
NorthWest	13.082	32.03	0.22	3710, 4030	0.80, 1.00	1.53, 1.71	3.23, 4.04
Arp 220 West							
W-Centre	57.191	11.66	20.3	5230	2.20	0.10	5.28
W-South	57.191	11.58	5.12	5230, 5360	1.03, 0.76	0.18, 0.14	3.37, 2.48
W-West	57.181	11.76	5.19	5140, 5230, 5340	1.30, 1.38, 1.75	0.22, 0.24, 0.29	10.06, 13.43
W-North	57.192	11.80	4.62	5090, 5280	1.30, 1.55	0.28, 0.29	3.89, 4.64
Arp 220 East							
E-East	57.265	11.53	6.18	5430	1.05	0.16	3.14
E-West	57.258	11.45	7.84	5160, 5320, 5400, 5540	2.20, 1.80, 1.75, 1.20	0.14 - 0.24	2.88 - 5.28

Notes: (a) Positions of IC 860 relative to RA = 13h:15m and Dec = 24°:37'. Positions of IRAS 15107+0724 relative to RA = 15h:13m and Dec = 07°:13'. Positions for Arp 220 relative to RA = 15h:34m and Dec = 23°:30'. (b) The continuum flux density represents a mean value across the emission region. (c) The line optical depth assumes exponential amplification of the background radio continuum.

emission originates in regions centred on the nuclei of the galaxies and that the emission results from masering amplification of the radio continuum by excited foreground molecular gas. The dominant H₂CO emission arises from a central (elongated) molecular structure of size 30 - 100 pc in a line of sight close to the peak of the continuum source, and also from some isolated star-formation regions, whose projected positions are also within a region defined by the radio contours. The central emission regions are consistent with a clumped masering medium in the central section of an edge-on molecular disk causing a hierarchy of emission structures from compact high-brightness to more extended lower-brightness components. Any emission from the outer regions of the disk is undetected because of the decreasing continuum flux. The central regions do not show a prominent velocity gradient because of the superposition of dominant point sources at different velocities superposed on a more extended structure. An elongated emission structure is also found in Sgr B2 as a string of six single maser features covering a linear distance of nearly 5 pc (Mehring et al. 1994; Qin et al. 2008), although there is no evidence yet of a more extended and diffuse component.

The formaldehyde emission at the West nucleus of Arp 220 coincides quite well with the presence of a compact circumnuclear disk as deduced from the OH MegaMaser and the CO and H I emission. The emission from its East nucleus may not be representative of the observed disk rotation, but it is still well-aligned with the larger-scale rotation structure (Sakamoto et al. 1999; Mundell et al. 2001; Baan 2007). In the cases of IC 860 and IR 15107+0724 no detailed molecular studies have yet been done. However, the observed formaldehyde emission structure is well aligned with the optical image of both galaxies, and in the case of IC 860 it also lies perpendicular to the extended relic continuum structure.

The weaker emission components found in IC 860 and IRAS 15107+0724 represent discrete star formation regions in the circumnuclear environment. The emission also results from amplification of the lower background continuum but they require higher amplifying optical depths than those in the nuclear region (Table 2). The estimated brightness temperatures of the emissions in the circumnuclear regions are slightly lower than those in the central regions, which gives a range for the observed temperatures between 6×10^3 K and 1.3×10^5 K. Such brightness temperatures confirm that the observed line emission results from masering activity and that these sources are indeed MegaMasers.

Except for the three galaxies considered here, single-dish spectra of nearby galaxies show absorption for both the 4.83 GHz K_a=1 and the 14.5 GHz K_a=2 transitions (Baan et al. 1993; Araya et al. 2004; Mangum et al. 2013). This would indicate that the ground state inversions are weak and possibly rare and that there is competition between emission and absorption in the 4.83 GHz line of most galaxies. As a result the integrated profiles may show evidence of absorption from extended regions, of localised emission, and possibly of localised re-absorption depending on the physical conditions of the intervening molecular material. The spectral results presented in this paper show some evidence of both narrow and broad absorption components, which could account for the differences when compared with the single-dish spectra (e.g. the feature at 3580 km s⁻¹ in the spectrum of IC 860). This spectral superposition is further supported by some recent single-dish 4.83 GHz H₂CO spectra of extragalactic sources that show clear evidence of emission components superposed on dominant absorption (see Mangum et al. 2013).

The occurrence of formaldehyde maser action remains rare in the Galaxy and in extragalactic sources. Although

there are many luminous infrared sources in the Galaxy and in extragalactic sources, only a small fraction of these are associated with H_2CO and also OH maser activity. Therefore, masering activity only happens during certain evolutionary stages when both the right pumping agent and the right molecular environment exist along a certain line of sight. As a result, the special conditions under which H_2CO masering action happens hold a key for understanding the sequence of events during starformation and starburst processes.

6.2 The H_2CO Pumping Environment

The establishment of maser action in four extragalactic sources again raises the issue of the responsible pumping mechanism for formaldehyde in Galactic and extragalactic sources. Early suggestions for pumping the formaldehyde molecules included radiative pumping by FIR radiation fields (e.g., Litvak 1969) and a pumping model using the free-free radio continuum (e.g., Boland & de Jong 1981). Free-free pumping can produce small level inversions but it does not explain the maser components discussed in this paper (Baan et al. 1986), and the formaldehyde masers in Sgr B2 (Mehring et al. 1994).

Collisional pumping models have been suggested based on H_2 and electron collisions (Araya et al. 2007) and shocks (Mehring et al. 1994; Hoffman et al. 2007; Araya et al. 2004). Collisional excitation with H_2 and radiative excitation by the free-free radio continuum radiation from a nearby ultra- or hyper-compact HII region can indeed invert the H_2CO $K_a = 1_{10-1_{11}}$ transition (van der Walt 2014). However, collisional pumping in shocks does not explain the simultaneous flaring of the H_2CO and 6.7 GHz Class II CH_3OH maser components of the Galactic source IRAS 18566+0408 (Araya et al. 2010).

The FIR radiation fields in the host galaxies of formaldehyde MM remain as the most viable pumping agent for extragalactic formaldehyde emitters and for Galactic sources. The FIR radiation fields are already found to be responsible for pumping the OH in Galactic sources and OH MM sources and they can also account for pumping many Class II maser transitions for Galactic methanol (Cragg et al. 2005) and naturally explains the flaring in IRAS 18566+0408. A early link between formaldehyde MM activity and FIR luminosity and spectral colour temperature has been established based on these galaxies (Baan et al. 1993; Araya et al. 2004), in analogy with similar relations for OH MM sources.

6.3 FIR Radiative Excitation of H_2CO

A radiative FIR pumping scenario for the formaldehyde 4.829 GHz $K_a = 1_{10-1_{11}}$ transition requires a certain temperature range for the prevailing FIR radiation field in order to achieve population inversions. The estimated FIR radiation blackbody temperatures are in the range of 40 to 65 K for the three galaxies (see Gao & Solomon 2004), which is also the range that results in pumping of the OH molecules. However, inversion of the formaldehyde $K_a = 1$ level cannot be achieved when the kinetic temperature (T_k) of the local environment is larger or equal to the blackbody temperature (T_d) of the dust FIR radiation (van der Walt 2014). There-

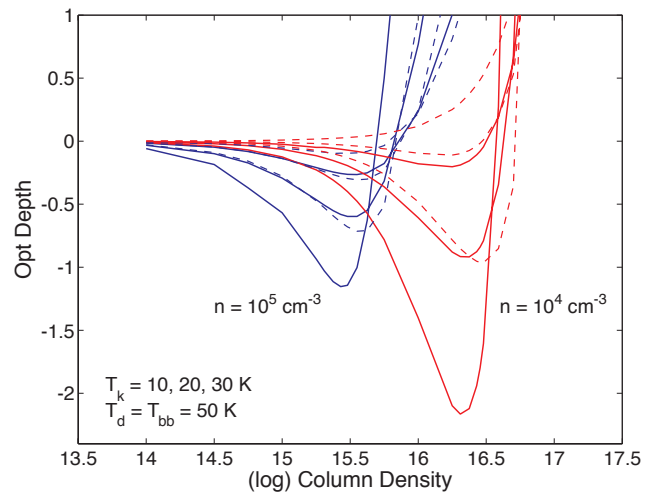


Figure 19. Inversion of the formaldehyde molecules by FIR radiative pumping. A representative dust temperature $T_d = 50$ K has been assumed to represent the FIR radiation field. The optical depth curves for the 4.83 GHz $K_a = 1$ transition are in solid lines and the curves for the 14.5 GHz $K_a = 2$ transition are in dashed lines. The two groups of curves are for two gas densities (blue for 10^5 cm^{-3} and red for 10^4 cm^{-3}) for three kinetic temperatures. The gains increase for lower gas densities and decrease for higher values of the kinetic temperature T_k .

fore, extragalactic environments with coupled dust and kinetic temperatures will only show absorption in both transitions combined with possible thermal emission in the $K_a = 1$ transition but will not show any maser activity (as seen by Mangum et al. 2013).

Simulations with the Radex facility (van der Tak et al. 2007) indicate that for local kinetic temperatures lower than the radiative temperature, inversions in both the $K_a = 1$ and $K_a = 2$ transitions can be achieved by FIR radiative pumping. This describes molecular environments with densities up to 10^5 cm^{-3} where the kinetic and dust temperatures are yet not coupled. The results of the simulations depicted in Figure 19 show that the attainable (negative) optical depth varies strongly with density and local kinetic temperature T_k and column density $N(\text{H}_2)$. Assuming a representative dust temperature of $T_d = 50$ K giving the blackbody FIR radiation field, the optimal densities are in the range of $n = 10^4 - 10^5 \text{ cm}^{-3}$. Weak or no inversions are found at both higher densities ($n = 10^6 \text{ cm}^{-3}$), where temperature coupling would result, and also at lower ($n = 10^3 \text{ cm}^{-3}$) densities. No inversion occurs when T_k becomes equal or higher than T_d . A maximum in the optical depth of $\tau_{4.8} = -2.2$ is found for a density of $n = 10^4 \text{ cm}^{-3}$ and a temperature difference $(T_d - T_k) = 40$ K; the gains decrease with a decreasing temperature $(T_d - T_k)$ difference.

Similar optical depth curves are found for the optical depth in the 14.5 GHz $K_a = 2_{11-2_{12}}$ transition except that the peak values typically scale as $\tau_{14.5} \approx 0.45 \tau_{4.8}$ (Fig. 19). However, no discernible maser emission has yet been detected in the 14.5 GHz transition in single-dish spectra of extragalactic sources (Mangum et al. 2013). This may be explained by the much lower gains found for the $K_a = 2$ transition and the disappearance of the inversion for smaller values

of the ($T_{bb} - T_k$) temperature difference. In the parameter range where both transitions could amplify the background radio continuum, a radio spectral index of $\alpha = -1$ and a (peak) assumed gain $\tau_{4.8} = -1.3$ will generate an expected emission line flux in the 14.5 GHz line that is only 9% of the 4.8 GHz emission line strength. Such 14.5 GHz line emission features may indeed go unidentified in the presence of a more dominant absorption component.

The evaluation of the FIR pumping of the formaldehyde in a non-coupled environment show that there is sufficient parameter space to provide the maser action observed in the four extragalactic sources. The optical depths deduced for the three sources (Table 2) lie within the range of attainable optical depths found with these pumping simulations. In addition, the non-coupled (dust-kinetic) temperature environment required for the pumping represents a plausible condition in the star-forming environments. The requirement of a non-coupled temperature environment may also define the transient environment that provides the window of opportunity for maser action and may explain the small numbers of observed formaldehyde masers.

7 CONCLUSION

The emissions in the formaldehyde ground state transition in the three galaxies, IC 860, IRAS 15107+0724, and Arp 220, are extended and show a range of structural scale sizes up to 100 pc. The brightness temperatures of the emission features ($T_b = 6 \times 10^3 - 1.3 \times 10^5$ K) falling within the contours of the nuclear radio continuum indicate that they are maser features resulting from amplification of the continuum background. A clumped foreground medium pumped by the FIR radiation fields will produce a hierarchy in the emission structure giving a combination of extended lower-brightness and compact higher-brightness maser components at a range of radial velocities.

The observed central emission regions are close to the peak of the nuclear continuum and are consistent with them being the front section of a larger scale disk structure in the galaxies. The central emission regions do not exhibit clear velocity gradients resulting from disk rotation, because dominant high-brightness components that contribute to the emission and the complex structure of the molecular ISM following a nuclear merger. The outer parts of the disk have not yet been detected because of the outward decrease of the continuum and possibly changing pumping conditions. In the case of Arp 220 it appears that the OH emission from the disk in the West nucleus actually straddles the observed formaldehyde emission (see [Rovilos et al. 2003](#)). In addition to the central emission regions, a number of less prominent and isolated regions have been found in all three sources. Most likely these are star formation regions with a higher amplifying gain superposed on weaker continuum components.

The pumping of the formaldehyde emission has been associated with the FIR radiation fields in the (U)LIRGs, which is analogous to the pumping scenarios for OH MMs. The FIR radiation field can invert the formaldehyde molecular population for a density range of $n = 10^4 - 10^5$ cm⁻³ when the local kinetic temperature T_k is lower than the blackbody temperature T_d of the radiation field. The ob-

served optical depths of the amplifying medium fall within the range predicted by the simulations of the pumping environment. In general, the observed optical depths are found to be relatively low, which would be consistent with the concept of low-gain amplification by an extended (more diffuse) and clumpy interstellar medium.

The current data for these extragalactic sources show some evidence for localised absorption in addition to the emission regions. The presence of absorption, localised emissions, and possible re-absorption in the ISM of the nuclear region may account for some of the spectral differences between the single-dish data and the interferometric results. The detection of localised emission will thus depend strongly on the beam size of the instrument and the other (unconfirmed) candidate formaldehyde emitters should also be studied at higher resolution.

The more extended emission found in formaldehyde in these galaxies provide a new view of the medium in these sources. In the past, maser studies have mostly concentrated on only the highest brightness components. However, it is becoming increasingly clear that a large fraction of the Galactic and also extragalactic OH, H₂CO and likely H₂O maser emission is extended and will be at least partially resolved in the highest resolution experiments. These extended maser regions may thus provide tools to study the structure and nature of the ISM in these sources in combination with other diagnostic tools.

The requirement for pumping of the formaldehyde by FIR radiation fields implies that cold material must still be present in the molecular ISM of the star-bursting nucleus. Considering that the ongoing star formation process continues to heat any regions in the ISM with a non-coupled dust and kinetic temperature regime, such regions will exist during a relatively small evolutionary time window during the relatively early stages of evolution of Galactic star formation and extragalactic starbursts. This may indicate that formaldehyde MM activity occurs at an earlier evolutionary stage than OH MM activity and this may also explain why only a few H₂CO MM have been found among the more extended OH MM sample.

For Galactic maser environments, a empirical time sequence has been suggested for maser activity with different flavours ([Ellingsen et al. 2007](#); [Breen et al. 2010](#)), which did not (yet) include formaldehyde masers. A similar sequence may now also exist for the maser activity during the evolution of star-bursting nuclei including OH, H₂CO, and also Class II CH₃OH masers.

ACKNOWLEDGEMENTS

This paper is written in memory of our friend James R. Cohen (1948 – 2006) with whom this project was started. WAB has been supported as a Visiting Professor of the Chinese Academy of Sciences (KJZD-EW-T01). WAB thanks the Shanghai Astronomical Observatory staff for their hospitality during the tenure. TA has been supported by the NSTC 973 Program (2013CB837900) and Shanghai Rising Star program. The e-MERLIN is a National Facility operated by the University of Manchester at Jodrell Bank Observatory on behalf of the UK Science and Technology Facilities Council (STFC). This research has made use of the

NASA/IPAC Extragalactic Database (NED) which is operated by the Jet Propulsion Laboratory, California Institute of Technology, under contract with the National Aeronautics and Space Administration. This publication makes use of data products from the Two Micron All Sky Survey, which is a joint project of the University of Massachusetts and the Infrared Processing and Analysis Center/California Institute of Technology, funded by the National Aeronautics and Space Administration and the National Science Foundation.

REFERENCES

- Araya, E., Baan, W.A., & Hofner, P., 2004, *ApJS*, 154, 541
 Araya, E., Hofner, P., & Goss, W. M. 2007, *IAU Symposium*, 242, 110
 Araya, E. D., Hofner, P., Goss, W. M., et al. 2008, *ApJs*, 178, 330
 Araya, E. D., Hofner, P., Goss, W. M., et al. 2010, *ApJ*, 717, L133
 Baan, W. A. 1985, *Nature*, 315, 26
 Baan, W. A. 1989, *ApJ*, 338, 804
 Baan, W. A. 2007, *IAU Symposium*, 242, 437
 Baan, W. A., van Gorkom, J. H., Schmelz, J. T., & Mirabel, I. F. 1987, *ApJ*, 313, 102
 Baan, W. A., Güsten, R., Haschick, A.D., 1986, *ApJ*, 305, 830
 Baan, W. A., & Haschick, A. D. 1984, *ApJ*, 279, 541
 Baan, W. A., & Haschick, A. D. 1995, *ApJ*, 454, 745
 Baan, W. A., Haschick, A. D., & Uglesich, R. 1993, *ApJ*, 415, 140
 Baan, W. A., Wood, P.A.D. & Haschick, A.D., 1982, *ApJ*, 260, L49
 Boland, W., & de Jong, T. 1981, *A&A*, 98, 149
 Braatz, J.A., Reid, M.J., Humphreys, E.M., et al. 2010, *ApJ*, 718, 657
 Breen, S. L., Ellingsen, S. P., Caswell, J. L., & Lewis, B. E. 2010, *MNRAS*, 401, 2219
 Chen, X., Ellingsen, S. P., Baan, W. A., et al., 2015, *ApJ*, 800, L2
 Claussen, M. J., Heiligman, G. M., Lo, K. Y., 1984, *Nature*, 310, 298
 Condon, J.J., 1992, *ARA&A*, 30, 575
 Cragg, D. M., Sobolev, A. M., & Godfrey, P. D. 2005, *MNRAS*, 360, 533
 Darling, J., & Giovanelli, R. 2002, *AJ*, 124, 100
 Downes, D., & Solomon, P. M. 1998, *ApJ*, 507, 615
 Ellingsen, S.P., Chen, X., Qiao, H.-H., et al., 2014, *ApJ*, 790, L28
 Ellingsen, S. P., Voronkov, M. A., Cragg, D. M., et al. 2007, *IAU Symposium*, 242, 213
 Gao, Y., & Solomon, P. M. 2004, *ApJ*, 606, 271
 Genzel, R., Lutz, D., Sturm, E., et al. 1998, *ApJ*, 498, 579
 Ginsburg, A., Walsh, A., Henkel, C. et al., 2015, *A&A*, 584, L7
 Haschick, A. D. & Baan, W. A., 1985, *Nature*, 314, 144
 Haschick, A. D., Baan, W. A., Schnepfs, M. H., et al. 1990, *ApJ*, 356, 149
 Haynes, M. P., Giovanelli, R., Herter, T., et al. 1997, *AJ*, 113, 1197
 Henkel, C., & Wilson, T. L. 1990, *A&A*, 229, 431
 Herrnstein, J.R., Moran, J.M., Greenhill, L.J., et al., 1997, *ApJ*, 475, L17
 Hoffman, I. M., Goss, W. M., & Palmer, P. 2007, *ApJ*, 654, 971
 Kellermann, K.I. & Owen, F.N., 1988, in Verschuur G.L., Kellermann K.I., eds, *Galactic and Extragalactic Astronomy*, Springer, Berlin, p.577
 Klöckner, H.-R., & Baan, W. A. 2004, *A&A*, 419, 887
 Kondratko, P. T., Greenhill, L. J., Moran, J. M., 2005, *ApJ*, 618, 618
 Kuo, C.Y., Braatz, J.A., Lo, K.Y., et al. 2015, *ApJ*, 800, 26
 Litvak, M. M. 1969, *ApJ*, 156, 471
 Middelberg, E., Agudo, I., Roy, A.L., Krichbaum, T.P., 2007, *MNRAS*, 377, 731
 Mangum, J. G., Darling, J., Menten, K. M., & Henkel, C. 2008, *ApJ*, 673, 832
 Mangum, J. G., Darling, J., Henkel, C., & Menten, K. M. 2013, *ApJ*, 766, 108
 Mehringer, D. M., Goss, W. M., & Palmer, P. 1994, *ApJ*, 434, 237
 Miyoshi, M., Moran, J., Herrnstein, J., et al., 1995, *Nature*, 373, 127
 Momjian, E., Romney, J. D., Carilli, C. L., & Troland, T. H. 2006, *ApJ*, 653, 1172
 Mundell, C. G., Ferruit, P., & Pedlar, A. 2001, *ApJ*, 560, 168
 Parra, R., Conway, J. E., Elitzur, M., & Pihlström, Y. M. 2005, *A&A*, 443, 383
 Qin, S.-L., Zhao, J.-H., Moran, J. M., et al. 2008, *ApJ*, 677, 353
 Rovilos, E., Diamond, P. J., Lonsdale, C. J., et al. 2003, *MNRAS*, 342, 373
 Sakamoto, K., Scoville, N. Z., Yun, M. S., et al. 1999, *ApJ*, 514, 68
 Sakamoto, K., Wang, J., Wiedner, M. C., et al. 2008, *ApJ*, 684, 957
 Schmelz, J. T., Baan, W. A., Haschick, A. D., & Eder, J. 1986, *AJ*, 92, 1291
 Skrutskie, M. F., et al. 2006, *AJ*, 131, 1163
 Slysh, V. I., Voronkov, M. A., Migenes, V., et al. 2001, *MNRAS*, 320, 217
 Smith, H. E., Lonsdale, C. J., Lonsdale, C. J., & Diamond, P. J. 1998, *ApJ*, 493, L17
 Spergel D.N. et al., 2007, *ApJS*, 170, 377
 van der Tak, F. F. S., Black, J. H., Schöier, F. L., et al. 2007, *A&A*, 468, 627
 van der Walt, D. J. 2014, *A&A*, 562, A68
 Wang, J.-Z., Zhang, Z.-Y. & Gao, Y., et al. 2014, *Nat. Commun.*, 5 6449
 Zhao, J.-H., & An, T. 2008, *Relativ. Astrophys.*, 966, 77